Hazard-Time Optimal Path Planning for Collaborative Air and Sea Drones

B. Schnitzler[a,b,c], P. J. Haley, Jr.[a], C. Mirabito[a], E. M. Mule[a], J.-M. Moschetta[b], D. Delahaye[c], A. Drouin[c] and
P. F. J. Lermusiaux[a,†]

[a] *Department of Mechanical Engineering, Massachusetts Institute of Technology (MIT), Cambridge, MA*
[b] *Department of Aerodynamics, Energy and Propulsion, Institut Supérieur de l'Aéronautique et de l'Espace, Toulouse, France*
[c] *OPTIM LAB, Ecole Nationale de l'Aviation Civile, Toulouse, France*
[†]Corresponding author: pierrel@mit.edu

Abstract—**General differential equations for multi-objective reachability and optimal planning are used to guide autonomous air and sea drones in hazard-time optimal missions. The vehicles minimize exposure to hazards and travel time, leveraging the dynamic environments with strong flows and steering clear of dynamic hazardous regions. We demonstrate the approach first with an autonomous air drone that crosses the Atlantic Ocean optimizing travel time using trade winds while avoiding hazardous rain storms in the inter-tropical convergence zone. We then consider an air drone that exploits winds and avoids hazardous rains to transport an ocean vehicle to a target destination. The ocean vehicle then completes its own hazard-time optimal mission, leveraging ocean currents and avoiding vessel-traffic hazards. In all cases, we predict hazard-time reachable sets, Pareto fronts, and optimal paths. The results highlight the benefits of considering hazards in optimal path planning.**

Index Terms—**Path planning, reachability analysis, ocean forecasting, weather forecasting, uncertainty, natural hazards, risk management.**

I. INTRODUCTION

The integrated optimization of autonomous air and marine platforms is becoming a grand challenge for the efficient utilization, monitoring, and protection of our environment and sustainable life on Earth. Applications include research, environmental monitoring, conservation, climate change mitigation, weather prediction, ocean forecasting, transport and distribution of goods, security, air-sea operations, communication, search and rescue, space and marine industry, and the blue economy. To achieve successful integrated air-sea autonomy in such applications, leveraging the complex dynamic environments, predicting hazards, and reducing risks is critical, especially for autonomous vehicles with limited actuation or high costs. Much progress has been achieved in the past decade in either marine or air path planning [1–5], Some efforts have included ocean risks [6–10] or air risks [11]. Integrated air-sea applications are very promising [12] but are not yet commonplace [13–23].

Path planning for autonomous vehicles in complex environments is an active area [24–26]. For planning in highly dynamic environments and reviews on the MIT-MSEAS (Multidisciplinary Simulation, Estimation, and Assimilation Systems) reachability and path planning, we refer to [2, 3, 27–29]. Fundamental differential equations and level-set schemes have been used for energy-optimal path planning [30, 31], coordinated, pursuit, and three-dimensional time-optimal path planning [32–35], stochastic path planning and risk optimization [10, 36–38], optimal harvesting and farming [39, 40], ship routing [41, 42], and real-time planning, adaptive sampling, and reachability forecasting with real autonomous vehicles at sea [43–47].

In this work, we apply general differential equations for exact multi-objective reachability and optimal planning [3, 29, 31, 48, 49] to guide autonomous air and sea drones towards their final location in minimum hazards and time. The vehicles leverage the dynamic environments with strong flows and steer clear of hazards along their path. For the first time, we combine weather, ocean, and hazard forecasting with dynamic multi-objective optimal control to obtain hazard-time reachable sets, Pareto fronts, and optimal paths. Given the predicted dynamic winds, currents, and hazard fields, the MIT-MSEAS theory and schemes provide optimal solutions for all arrival times and cumulative hazard tolerances.

Our first application considers airborne drones and hazard-time optimal long-distance missions with rain avoidance. It is motivated by ISAE-SUPAERO's "Mermoz challenge" which consists of building a hydrogen-power Unmanned Air Vehicle (UAV) to cross the Atlantic between Dakar, Senegal, and Natal, Brazil, thus achieving the same route as air mail pioneer Jean Mermoz while drastically reducing greenhouse gas emissions [50, 51]. For such missions, it is well known that the intertropical convergence zone on the drone's path is challenging because it often features many thunderstorms. There is thus a need to account for hazards due to storms for more risk-averse planning. A main goal is to provide time-optimal storm-avoiding paths, optimally leveraging Atlantic winds for varied levels of cumulative storm hazards.

The second application is a hazard-time optimal collaborative mission between air and sea drones. The air drone transports the ocean vehicle optimally to a target location exploiting winds and avoiding storms, and the ocean vehicle subsequently completes its mission leveraging currents and avoiding vessel traffic hazards. It is motivated by missions off the US East Coast, around the New England Seamounts region [52]. The air drone leaves land carrying the sea drone in stormy conditions, transporting it in fastest time to its start location. The sea drone is dropped and travels to the north of the New England Seamounts in fastest time exploiting ocean currents, collecting data en route to rendezvous with a research vessel in the area, and limiting vessel traffic risks. Hazard-

time Pareto-fronts are predicted for both the air transport and marine missions, providing all trade-off optimal solutions between travel time and exposure to hazards.

In what follows, in section II, we describe the theory, algorithms, and numerical schemes for hazard-time reachability and path planning. In section III-A, we apply the theory and schemes to rain-hazard and time optimal reachability analysis for air drones, In section III-B, we present results for an air-sea collaboration. It consists of a rain-hazard and time optimal transport of a sea drone by an air drone followed by a traffic-hazard and time optimal mission by the sea drone. Finally, we conclude in section IV.

II. THEORY AND SCHEMES

A. Governing Equations

Our generic problem is that of computing the paths of drones that minimize both travel time in a dynamic flow environment $\boldsymbol{V}(\boldsymbol{x}, t)$ and accumulated exposure to a dynamic hazard field $\mathfrak{h}(\boldsymbol{x}, t)$. Indeed we want to predict the reachable sets in the spatial and cumulative hazard dimensions, and all Pareto-optimal paths for the corresponding two costs, travel time and cumulative hazards. The application domains involve collaborative air and sea drones, but the theory applies to many other domains.

In our notation, the three-dimensional (3D) position vector in the physical environment space is denoted by $\boldsymbol{x}$ and time by t. For the vehicle, the cost due to hazards is a measure of the accumulation of the instantaneous hazards $\mathfrak{h}$. We denote the corresponding integral over time or accumulated hazard level by η. This variable η is also referred to as cumulative hazard function [53, 54].

For the dynamics in the physical space, the spatiotemporal scales of our missions are much larger than the vehicle scales. We thus assume that the vehicle is in mechanical equilibrium at all times and evolves through the kinematic equation in the spatial domain, i.e.,

$$\frac{\mathrm{d}\boldsymbol{x}}{\mathrm{d}t} = v_{\max}\boldsymbol{h}(t) + \boldsymbol{V}(\boldsymbol{x}, t) \qquad (1)$$

where $v(t) \in [0, v_{\max}]$ is the nominal propulsion speed, $v_{\max}$ its maximum or desired cruising speed, and $\boldsymbol{h}(t)$ the heading of the vehicle. For the dynamics in the cumulative hazard space, we assume that the measure of the accumulation of instantaneous hazards $\mathfrak{h}$ is a known function of space and time, such that its integral over time is the cumulative hazard η, i.e.,

$$\frac{\mathrm{d}\eta}{\mathrm{d}t} = \mathfrak{h}(\boldsymbol{x}, t). \qquad (2)$$

We note that different hazards can be kept separate and not combined, in which case η is a vector of cumulative hazards. Without loss of generality, η is here set to be a scalar. To account for it, we add it as a new dimension [31, 49]. We thus define the augmented state space of the spatial position and cumulative hazard, $(\boldsymbol{x}, \eta)$. In this $(\boldsymbol{x}, \eta)$ space, solving our problem consists in computing the augmented reachable set for the vehicle, i.e., the set of all values $(\boldsymbol{x}, \eta)$ that are reachable at some time t. We represent the reachable set by a scalar function $\phi(\boldsymbol{x}, \eta, t)$ whose subzero level set is the

reachable set at time t. This level set function (value function) is governed by the following exact Hamilton-Jacobi-Bellman PDE [31, 48],

$$\frac{\partial \phi}{\partial t} + v_{\max} \left\| \frac{\partial \phi}{\partial \boldsymbol{x}} \right\| + \boldsymbol{V}(\boldsymbol{x}, t) \cdot \frac{\partial \phi}{\partial \boldsymbol{x}} + \mathfrak{h}(\boldsymbol{x}, t)\frac{\partial \phi}{\partial \eta} = 0 , \quad (3)$$

which is generally defined in a 5D space (time, physical space, and cumulative hazard).

In our applications, the physical space is the 2D planar space $\boldsymbol{x} = (x, y)$. The instantaneous hazard field $\mathfrak{h}$ is either a spatiotemporal function of the hazardous precipitation (rain) field $\mathfrak{p}(\boldsymbol{x}, t)$, i.e., $\mathfrak{h} = \mathfrak{h}(\boldsymbol{x}, t, \mathfrak{p})$, a function of hazardous ocean current or wind fields $\boldsymbol{V}(\boldsymbol{x}, t)$, i.e., $\mathfrak{h} = \mathfrak{h}(\boldsymbol{x}, t, \boldsymbol{V})$, or a function of other variables such as expected vessel traffic density field $\rho_v(\boldsymbol{x}, t)$, i.e., $\mathfrak{h} = \mathfrak{h}(\boldsymbol{x}, t, \rho_v)$.

B. Computational Schemes

For each of the applications, we scale variables and inputs (domain boundaries, $\boldsymbol{V}(\boldsymbol{x}, t)$, $\mathfrak{h}(\boldsymbol{x}, t)$) such that the governing equations are non-dimensional and the problem is numerically well conditioned [35], e.g., the coordinate variables x, y, η are of an order of magnitude of 1. To compute the values of $\phi(\boldsymbol{x}, \eta, t)$, we initialize ϕ to ϕ_0, the signed distance to a ball centered at the origin $(\boldsymbol{x}_0, 0)$ with radius ρ_{init}

$$\phi_0(\boldsymbol{x}, \eta) := \left\| \begin{pmatrix} \boldsymbol{x} \\ \eta \end{pmatrix} - \begin{pmatrix} \boldsymbol{x}_0 \\ 0 \end{pmatrix} \right\| - \rho_{\text{init}}$$

In theory, the perfect initialization would be obtained for $\rho_{\text{init}} = 0$, but in practice, this would lead to no grid point being part of the subzero level set, so the numerical scheme could not compute the evolution of the latter. Instead, we set ρ_{init} to be twice the grid spacing and integrate the initial solution analytically from the origin until the circle ρ_{init}.

To compute the evolution of the subzero level set, we use a second-order Essentially Non-Oscillatory (ENO) scheme in space and a second-order scheme in time [31].

Once $\phi(\boldsymbol{x}, \eta, t)$ is computed, we obtain the Pareto-optimal ways to reach any destination point $\boldsymbol{x}_f$ in physical space and cumulative hazard level η. If $\boldsymbol{x}_f$ is reachable, we have the minimum duration $\tau^\star$ to reach $\boldsymbol{x}_f$ as

$$\tau^\star := \min\left\{ \tau \mid \exists \eta \in [\eta_{\min}, \eta_{\max}], \quad \phi(\boldsymbol{x}_f, \eta, \tau) = 0 \right\} .$$

It is the first time the zero level set of ϕ reaches the segment $\{(\boldsymbol{x}_f, \eta) \mid \eta \in [\eta_{\min}, \eta_{\max}]\}$ in the augmented state space.

Then, for larger durations $\tau \geq \tau^\star$, we can extract the minimum possible amount of hazard to reach the destination point in the exact given duration, i.e.,

$$\eta^\star(\tau) = \min\left\{ \eta \mid \phi(\boldsymbol{x}_f, \eta, \tau) = 0 \right\} .$$

The collection of points

$$\{(\tau, \eta^\star(\tau)) \mid \tau \geq \tau^\star\}$$

is then the hazard-minimal curve to reach $\boldsymbol{x}_f$. We can deduce Pareto-optimal couples $(\tau, \eta^\star(\tau))$ from this curve by removing Pareto-dominated points. An example of such a curve is given in Fig. 1.

When a designated couple $(\tau, \eta^\star(\tau))$ is chosen, one may then ask how to compute a trajectory that links the starting point in the augmented state space $(\boldsymbol{x}_0, 0)$ to the destination point with this performance. To solve for this, we perform
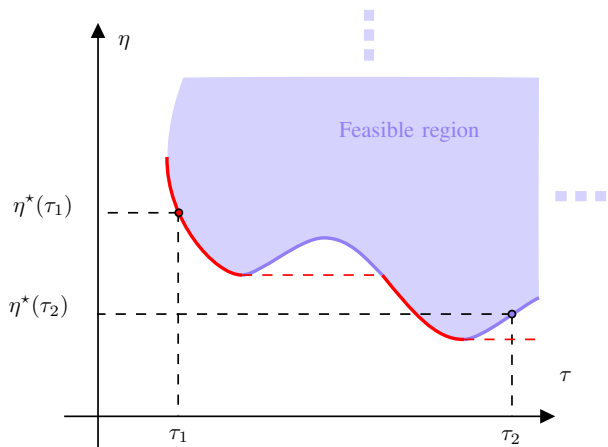
Fig. 1: Hazard-time solution domain: feasible region and Pareto front. The shaded region corresponds to feasible solutions (τ, η). The thicker lower curve contains the pairs $(\tau, \eta^\star(\tau))$ corresponding to hazard-only minimizing trajectories, for each time τ. The red portion of the curve encompasses the hazard-time optimal or so-called Pareto-optimal solutions. The red dot $(\tau_1, \eta^\star(\tau_1))$ corresponds to a Pareto-optimal hazard-time pair while the purple dot $(\tau_2, \eta^\star(\tau_2))$ is Pareto-dominated, because there are trajectories arriving earlier with the same amount of accumulated hazard.

backtracking of trajectories using the gradient of ϕ. Using Eqs. (1-2), the backtracking ODEs in the augmented space are

$$\begin{cases} \dfrac{\mathrm{d}\boldsymbol{x}}{\mathrm{d}t} &= -v_{\max}\,\boldsymbol{h}^\star(\boldsymbol{x}, \eta, t) - \boldsymbol{V}(\boldsymbol{x}, t) \\ \dfrac{\mathrm{d}\eta}{\mathrm{d}t} &= -\mathfrak{h}(\boldsymbol{x}, t) \end{cases} \quad (4)$$

where $\boldsymbol{h}^\star(\boldsymbol{x}, \eta, t) := \left\| \frac{\partial \phi}{\partial \boldsymbol{x}}_{(\boldsymbol{x}, \eta, t)} \right\|^{-1} \frac{\partial \phi}{\partial \boldsymbol{x}}_{(\boldsymbol{x}, \eta, t)}$. These ODEs are initialized at time τ at position $(\boldsymbol{x}_f, \eta^\star(\tau))$. After performing the integration, one obtains a trajectory $(\boldsymbol{x}(\cdot), \eta(\cdot))$ from $(\boldsymbol{x}_0, 0)$ at $t = 0$ to $(\tau, \eta^\star(\tau))$ at $t = \tau$.

III. APPLICATIONS

A. Rain-Avoidance–Time Optimal Planning for Air Drones

The first mission consists of the crossing of the Atlantic between Dakar, Senegal, and Natal, Brazil, by a UAV with a cruising speed of $23\,\mathrm{m\,s^{-1}}$, $100\,\mathrm{m}$ above sea level. In this application, we predict optimal trajectories for such an airborne drone providing all possible trade-offs between travel time by exploiting instantaneous winds and hazards by limiting thunderstorm exposure. Most precisely for the latter, we select the rain field as a proxy for thunderstorms. Since thunderstorms commonly imply heavy rain, this choice is conservative in avoiding rain, possibly avoiding zones with only some rain but no thunderstorms. Another reason why we work with rain data rather than thunderstorm data is because the former is available in practically all weather products. For instance, rain is available in both ERA5 reanalysis data and ECMWF forecasts, two open-access data sources. This is not the case for parameters such as the number of lightning per surface unit area or the cloud coverage, which may be found in reanalyses but not necessarily in forecasts.

We thus take $\mathfrak{h}(\boldsymbol{x}, t, \mathfrak{p}(\boldsymbol{x}, t)) := a\,\mathfrak{p}(\boldsymbol{x}, t)$, where $\mathfrak{p}(\boldsymbol{x}, t)$ is the ECMWF 3h-accumulated rain forecast and a is a dimensional scaling parameter that relates the hazards to the drone as a function of the rain. Of course, other parameterizations of instantaneous hazards can be selected such as higher-order polynomials or other functions that increase hazards nonlinearly as the rain increases and are representatives of the risks to the air drone. For our specific application, we select a linear function of the 3h-accumulated rain and the ECMWF rain forecast issued on 2024-04-25 00:00Z. For the environmental flows $\boldsymbol{V}(\boldsymbol{x}, t)$, we employ the corresponding ECMWF wind forecast. Snapshots of these wind and rain fields are given in Fig. 2, clearly indicating the prevailing northeasterly trade winds and strong rain storms around the equator.
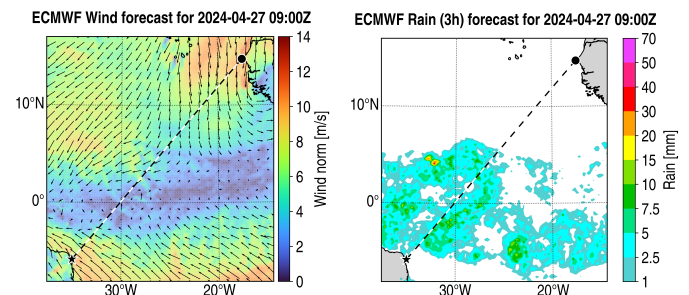

Fig. 2: Instantaneous wind (100 m) and 3h-accumulated rain forecast snapshots from ECMWF. The path planning start point is depicted as a black circle, the endpoint as a black star, and between them the shortest-distance great circle is drawn.

The air drone takes off on 2024-04-27, at 15:00Z. It flies to the destination in the fastest possible time leveraging winds while avoiding high accumulated exposure to rain. Example key questions include: Will rain avoidance lead to significantly different paths from the fastest ones, both in travel time and shape of the path? What are all of the hazard-time optimal paths so that the drone operators can select the paths most appropriate to their level of risk and desired arrival time? What is the cumulative hazard that corresponds to the fastest time path? Is there an arrival time that avoids the forecast rain? Our hazard-time optimal analysis provides clear answers to all such questions.

Solving eq. (3) in its non-dimensional normalized form [35], we obtain the hazard-time reachable set and reachability front. We can then compute all rain-travel-time Pareto-optimal paths solving the backtracking eqs. (4). They minimize the accumulated rain and travel time and include the overall minimum travel time path, i.e., the path that minimizes travel time by optimally exploiting the wind field while ignoring rain. In Fig. 3, we display the evolution of the reachability front, which is the zero-level set of the value function ϕ in the cumulative hazard η and physical space (x, y). In Fig. 3a, the reachable set started propagating from its initial position. There is no rain around the starting point so the shape of the reachable set is governed by time-optimal trajectories in the winds. The width of the reachable set on this frame in the hazard
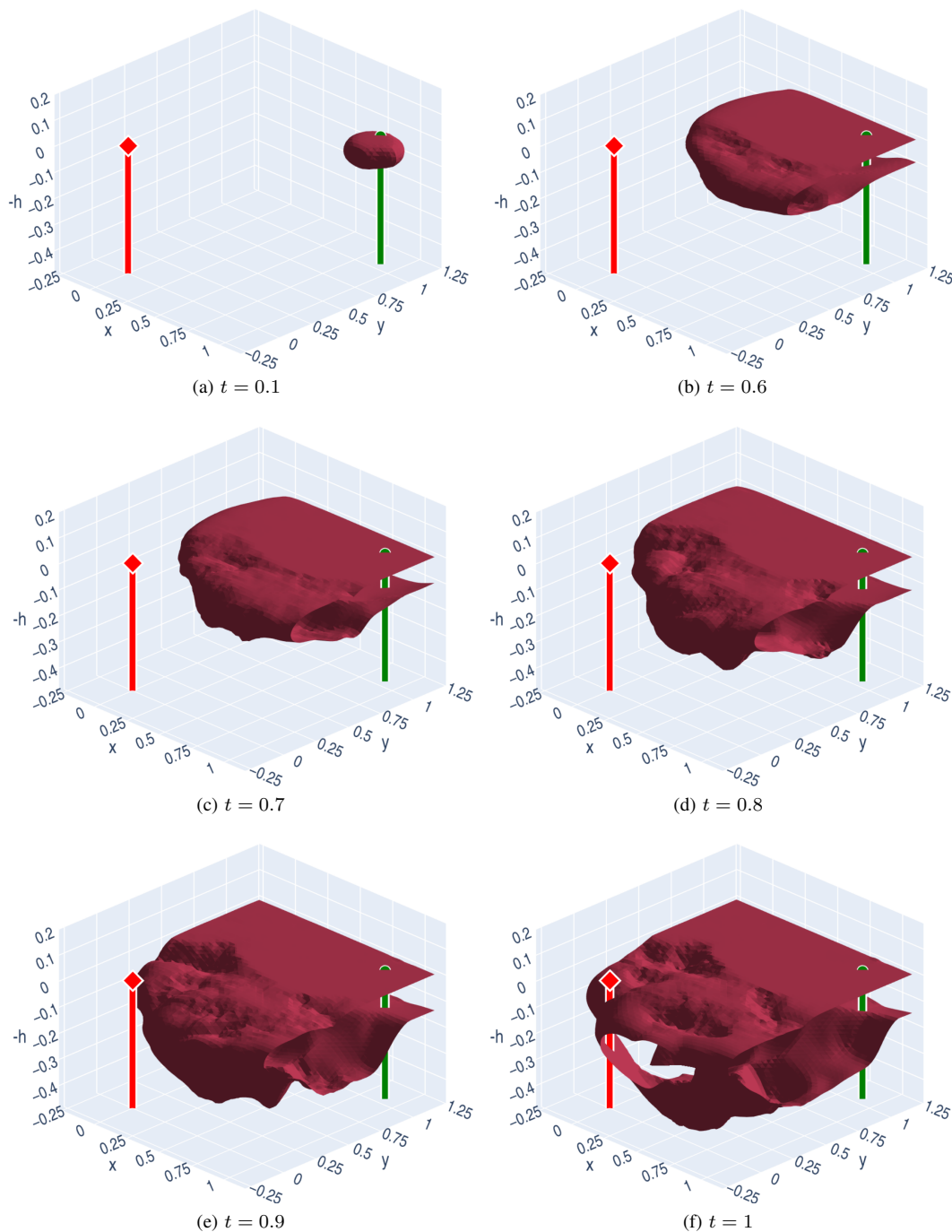
Fig. 3: Hazard-time optimal air drone crossing the Atlantic: Reachable set evolution in the augmented state space (x, y, η). The hazard dimension is flipped (the η axis is indeed a $-\eta$ axis) to more directly visualize the hazard-minimizing part of the reachable set; in these graphs, the minimum hazards are thus at the top of the 3D reachable set. The start location is depicted as a green dot with a green line in the direction of increasing hazards. Similarly, the final location is depicted as a red diamond with a red line in the same direction. All times t, space (x, y), and cumulative hazard η are non-dimensional.

direction remains twice ρ_{init} (Sec. II-B). At $t = 0.6$ (Fig. 3b), the reachable set has reached the rain zone and hazards started to accumulate: the front there changed appearance from flat to rough, reflecting the rain patterns. As stronger hazardous rain is encountered, the reachable set goes down (Fig. 3c). In Figs. 3d–e, the part of the front that is the closest to the

red line corresponds to trajectories close to the time-optimal ones. This part of the front accumulates much hazard and is thus much lower than the original flat portion of the front. Finally, in Fig. 3f, we observe how slower but less hazardous trajectories are found within portions of the front intersecting the destination red line with lower accumulated hazard.
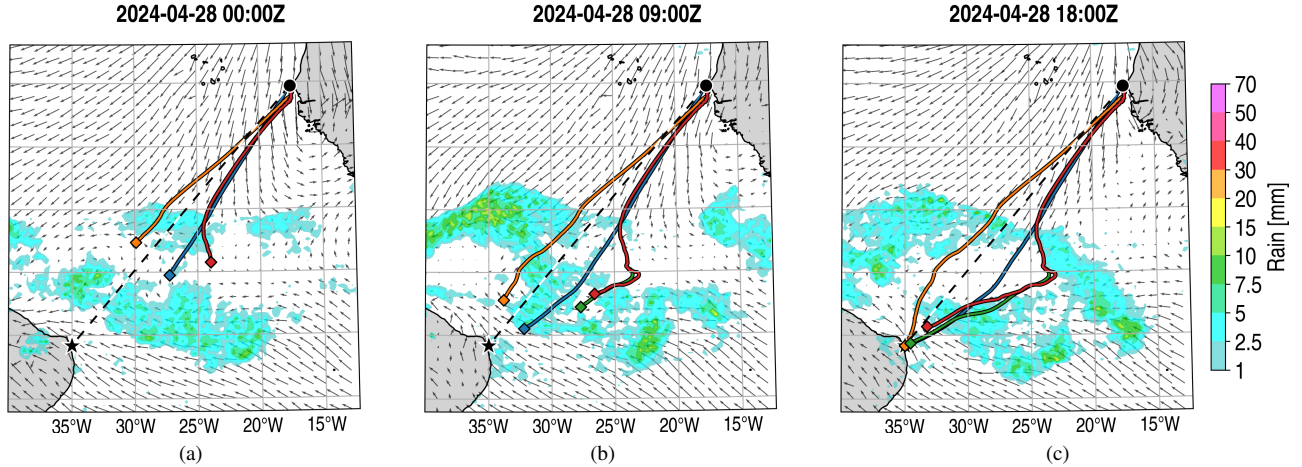
4

Fig. 4: Hazard-time optimal air drone crossing the Atlantic: (a, b, c) Snapshots at three different times of four hazard-time Pareto-optimal trajectories overlaid on the corresponding rain and wind fields. The paths are colored according to their arrival time and cumulative rain hazard level, as shown in Fig. 5.

In Fig. 4, we show three snapshots of hazard-time optimal paths for four optimal travel times and cumulative hazards, the first path (blue) being the strictly time-optimal path (ignoring rain). We find that, while the pure time-optimal path rushes through the rain, other trajectories computed for longer travel time but lower exposure to hazard manage to avoid heavy rains. We also observe that winds are quite steady, but the rain field evolves quickly. The time-optimal trajectory in blue crosses a zone of high precipitation (Fig. 4b). The orange trajectory encounters less rain by taking a route north of the great circle between Dakar and Natal. The green and red trajectories deviate even more from the great circle path: while the rain exposure is not significant enough, they both first follow the strictly time-optimal path, but then leave it (Fig. 4a) and meander along an evolving, quiet zone (Fig. 4b) with less rain before reaching the final destination (Fig. 4c).

In Fig. 5, we show Pareto-optimal travel times and cumulative hazards. The values are given in table I. We find that a moderate increase in travel time can result in a significant decrease in exposure to hazards. For example, simply changing from the strictly time-optimal, blue trajectory to the orange one gives a reduction in rain hazards of 54%, while increasing the travel time by only 5.9%. The table shows the operational benefit of our joint hazard-time trajectory optimization by providing the operator with a variety of optimal paths with different performance. The operator or the drone itself can select its preferred optimal path depending on the criticality of being on time compared to being exposed to hazards.

In Fig. 5, we also show non-Pareto-optimal portions on the hazard-time graph (dashed line). This confirms that increasing the travel time is not a sufficient condition for lowering exposure to rain. For instance, if heavy rain is barring the road, any trajectory passing through to ensure a given travel time will inevitably have a high accumulated hazard when reaching the destination.
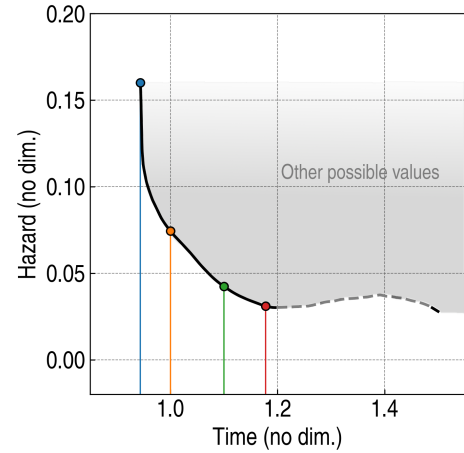

Fig. 5: Hazard-time optimal air drone crossing the Atlantic: Minimum total cumulative rain hazard for various travel times for the Dakar-Natal crossing. Solid curves are Pareto optimal values. The four colored dots on the Pareto-front correspond to paths shown with their color in Fig. 4.

Travel duration τ		Total hazard $\eta^\star(\tau)$	
0.944	-	0.160	-
1.000	+5.9%	0.0743	-54%
1.100	+17%	0.0423	-74%
1.178	+25%	0.0310	-81%

TABLE I: Hazard-time optimal air drone crossing the Atlantic: Travel times and cumulative rain hazards for the four backtracked trajectories of the Dakar-Natal air mission. Both travel time and hazard are non-dimensionalized variables which have no units.

B. Hazard-time Optimal Air-Sea collaboration

This second mission consists of two parts. First, a transport air drone departs from Boston, MA on 2024-02-17, 10:00 UTC, and drops a sea drone in the region of the New England

Seamounts in fastest time, taking advantage of favorable winds and avoiding unfavorable ones. However, it faces forecast stormy conditions with high wind bursts and hazardous rain that require a trade-off between exposure to hazards and travel time. Second, once the sea drone has been dropped, its mission is to proceed to the north of the Atlantis II seamount in fastest time in accord with dynamic ocean currents. However, it needs to limit its exposure to hazards from expected vessel traffic, hence a second ocean hazard-time optimal reachability analysis is completed.

For this collaborative air-sea mission, example key questions include: Can the transport air drone reach its final location soon enough for the sea drone while avoiding regions with too strong storms? What are all the rain-hazard, vessel-traffic-hazard, and time optimal choices for the air and sea drone operators? What are the optimal sea drone paths that collect the desired ocean data in fastest time while minimizing vessel-traffic hazards? Our collaborative hazard-time optimal analysis can answer all such questions.

1) Rain-hazard and time optimal transport air drone: For our application, for the transport by the air drone, we employ data from the ERA5 atmospheric reanalysis from the European Center for Medium-range Weather Forecasts (ECMWF), accessible through the Copernicus Climate Data Store (CDS). For the environmental flows $V(x, t)$, we extract the hourly 100 m wind field, and for the rain hazard, the 1h-accumulated rain field $\mathfrak{p}(x, t)$. Once again, we define the instantaneous hazard from the rain field as $\mathfrak{h}(x, t, \mathfrak{p}(x, t)) := a\,\mathfrak{p}(x, t)$ where the dimensional scaling parameter a ensures that the resulting $\mathfrak{h}$ represents the instantaneous hazard due to rain. We depict the wind and rain conditions at 2024-02-17 18:00 UTC in Fig. 6. There is a storm with counter clock-wise winds passing through the region, creating favorable conditions for trajectories that bend southward. The maximum of precipitation passes through the shortest-distance great circle between the start and destination locations, also encouraging trajectories to avoid this shortest-distance path to the destination. The dynamic behavior can also be seen in Fig. 7.
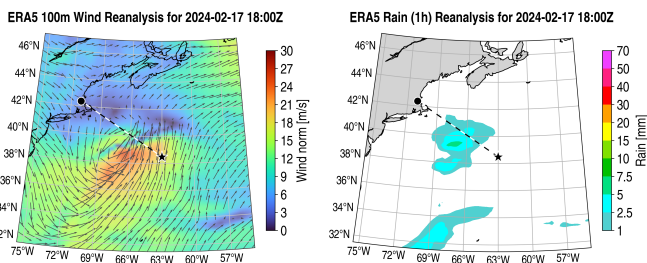

Fig. 6: Instantaneous wind (100 m) and rain snapshots from the ERA5 reanalysis. The path planning start point is depicted as a black circle, the endpoint as a black star, and between them the shortest-distance great circle is drawn.

We again solve eq. (3) in its non-dimensional normalized form [35] to obtain the hazard-time reachability front and the Pareto front, and then the backtracking eqs. (4) to highlight Pareto-optimal paths to the destination. Four of these Pareto-

optimal trajectories are depicted in Fig. 7. The corresponding Pareto front is shown in Fig. 8.

As shown in Figs. 7-8, the presence of a storm featuring high winds accelerating the vehicle but also much rain entails a clear variation in the amount of total hazard depending on the desired travel time. From the monotonic Pareto front (Fig. 8), trajectories going the fastest are the most exposed to the rain. Other trajectories accepting longer travel times can follow the wake of the storm, thus avoiding most of the rain. What is noticeable is that with an order of magnitude of $23\,\mathrm{m/s}$ for the speed of the air drone, optimal trajectories are bending significantly south, taking the western side of the storm and differing much from the great circle joining the start to the destination. For example, the fastest blue trajectory is much longer than this shortest distance. Nonetheless, it encounters rain in the back of the storm (Fig. 7b-c). Other Pareto-optimal trajectories that don't take full advantage of the strong winds can drastically reduce their total exposure to this rain hazard by remaining in the dryer side of the storm while still arriving only a bit later. For example, the orange and green trajectories (Fig. 7) reduce the cumulative rain hazard by about 100 to 500 percent while only increasing travel time by 10 to 20 percent, see Fig. 8.

2) Vessel-traffic-hazard and time optimal sea drone: Once the air drone reaches its destination at approximately 2024-02-18 01:00 UTC, it drops a sea drone in the vicinity of the New England Seamounts. This sea drone then travels along the ocean surface at a nominal speed of $3\,\mathrm{m/s}$ to a location north of the Atlantis II seamount in fastest time to collect data and rendezvous with a research vessel in the area. During this journey, it faces a trade-off between travel time and exposures to expected hazards due to interfering vessel traffic.

For the ocean environmental flows $V(x, t)$, we utilize our ocean current hindcasts from the MIT-MSEAS primitive-equation ocean model [46, 55, 56]. For the surface vessel traffic hazard, we employ the historical traffic density data from the Global Maritime Traffic Density Service (GMTDS) in terms of hours of vessel traffic per square kilometer. We thus define the instantaneous hazard from this expected vessel traffic density field $\rho_v(x, t)$ as the linear function $\mathfrak{h}(x, t, \rho_v(x, t)) := b\,\rho_v(x, t)$ where the dimensional scaling parameter b ensures that the resulting $\mathfrak{h}$ represents the instantaneous hazard due to vessel traffic. As noted for the rain hazards (see Sect. III-A), other parameterizations of instantaneous vessel hazards can be selected such as higher-order polynomials or other functions that increase hazards nonlinearly as vessel traffic density increases and are representatives of the risks to the chosen ocean vehicle. In general, ρ_v can be data that varies with the time of the day or a fully dynamic forecast $\rho_v(x, t)$. In our example, we utilized the historical time-averaged vessel traffic GMTDS data so ρ_v is a spatial field steady in time.

We solve eq. (3) in a non-dimensional normalized form [35] to obtain the hazard-time reachability front and all Pareto-optimal solutions. We then solve the backtracking eqs. (4) to highlight Pareto-optimal paths the destination. Three of these Pareto-optimal trajectories are depicted in Fig. 9. The
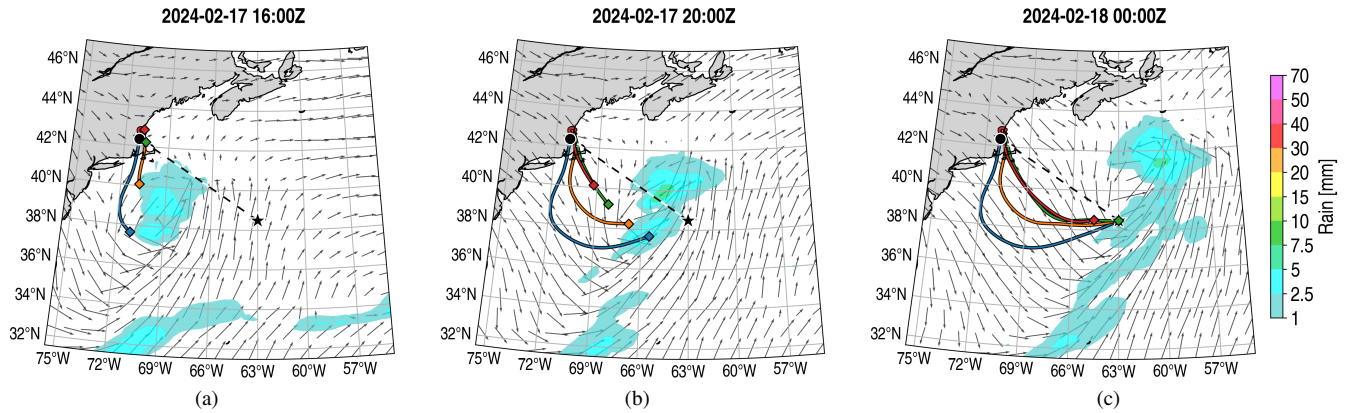
Fig. 7: Hazard-time optimal air-sea collaboration. Air drone reaching the New England Seamounts in hazard-time optimal fashion, transporting the sea drone: (a, b, c) Snapshots of four hazard-time Pareto-optimal trajectories, overlaid on rain and wind fields. The paths are colored according to their arrival time and cumulative rain-hazard level, as shown in Fig. 8.
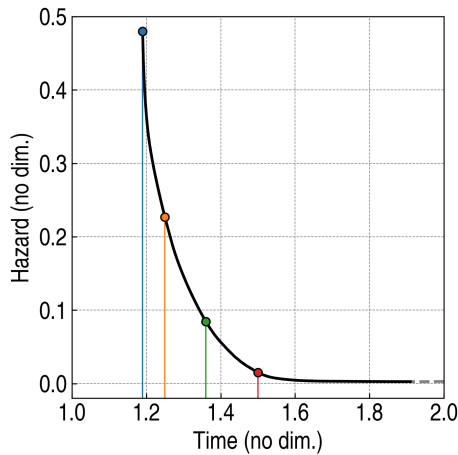

Fig. 8: Hazard-time optimal air-sea collaboration: Minimum total cumulative rain-hazard for various travel times for the air drone transporting a sea drone to the New England Seamounts. Solid curves are Pareto optimal values. The four colored dots on the Pareto-front correspond to paths shown with their color in Fig. 7.
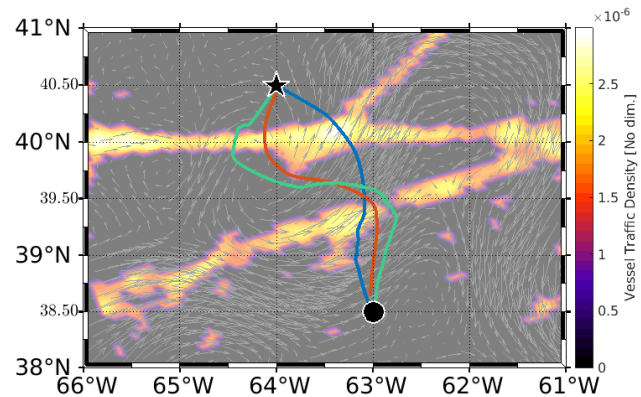
Fig. 9: Hazard-time optimal air-sea collaboration: Pareto-optimal trajectories for the sea drone, overlaid on the non-dimensional traffic density field and MIT-MSEAS forecast ocean current vectors. The three paths are colored according to their arrival time and cumulative traffic-hazard level, as shown in Fig. 10.

corresponding traffic-hazard and time Pareto front is shown in Fig. 10.

As shown in Fig. 9, the sea drone is operating in an area with several historical transit lanes, visible in yellow and white in the figure background. A fast Pareto-optimal path (shown in blue) takes advantage of the forecast currents but goes across some high-density and wide-double vessel traffic lanes hence has a high cumulative hazard, as shown in Fig. 10. Two other Pareto-optimal paths with lower cumulative hazard (shown in red and green) minimize hazard-time by first crossing the southern transit lane at the area of lowest historical traffic density at approximately [63°W, 39.5°N]. Both of the lower hazard paths then move to the west. By doing so, the ocean vehicle is only required to cross one additional transit lane (instead of a wide double-lane to the east), and avoids the large intersection that occurs near [63.5°W, 40°N].

IV. CONCLUSIONS

We applied the MIT-MSEAS general partial differential equations for exact multi-objective reachability and optimal planning to guide autonomous air and sea drones in hazard-time optimal missions. The vehicles minimize travel time and exposure to hazards, leveraging the dynamic environments with strong flows and steering clear of hazards along their paths. Our approach rigorously combines weather, ocean, and hazard forecasting with dynamic multi-objective optimal control to predict hazard-time reachable sets, Pareto fronts, and optimal paths for all computed cumulative hazard and arrival times.

Our first hazard-time optimal path planning application consisted of an autonomous air drone that crossed the Atlantic Ocean optimizing travel time using trade winds while avoiding
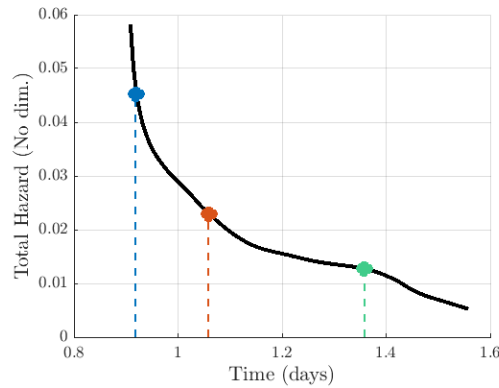
7

Fig. 10: Hazard-time optimal air-sea collaboration: Minimum total cumulative traffic-hazard for various travel times for the sea drone. Solid curves are Pareto optimal values (Pareto front). The three colored dots on the Pareto-front correspond to paths shown with their color in Fig. 9.

hazardous rain storms. The second was the hazard-time optimal transport of an ocean vehicle by an air drone followed by a hazard-time optimal ocean mission. Exploiting winds and avoiding hazardous rains, the transport air drone travels to a target location where it drops the ocean vehicle. The ocean vehicle then completes its mission in the fastest time, leveraging ocean currents and avoiding vessel-traffic hazards.

Our methodology highlights the benefits of considering hazards in optimal path planning. It provides the operators and the autonomous vehicles with a variety of Pareto-optimal trajectories with different performance levels reflecting the risks and multiple objectives of real operations [37, 49]. Compared to heuristics, our differential equations govern the multi-objective reachable set and globally Pareto-optimal paths exactly. Given environmental flows and hazard fields forecasts from operational data and dynamical modeling systems, their numerical integration provides all Pareto-optimal solutions up to the bounded errors of computational schemes.

Future promising hazard-time optimal missions include experiments with real air and sea drones [43, 45, 47], advanced operations with multi-vehicles and coordinated teams [32, 57, 58], and onboard implementations so that vehicles can directly assimilate data and run their own planning forecasts and optimal controls [59–61]. Considering other types of hazards, more advanced hazard modeling, and other air-sea applications including air-sea-space applications would be beneficial [19, 62, 63]. Optimal path planning under hazards could also involve probabilistic hazards and risks modeling [10, 36, 37], leading to stochastic hazard-time path planning. Finally, multi-time and multi-field reachability will be useful in many applications including efficient capabilities for frequent re-planning [29, 31, 49].

REFERENCES

[1] Z. Zeng, L. Lian, K. Sammut, F. He, Y. Tang, and A. Lammas, "A survey on path planning for persistent autonomy of autonomous underwater vehicles," *Ocean Engineering*, vol. 110, pp. 303–313, 2015.

[2] P. F. J. Lermusiaux, T. Lolla, P. J. Haley, Jr., K. Yigit, M. P. Ueckermann, T. Sondergaard, and W. G. Leslie, "Science of autonomy: Time-optimal path planning and adaptive sampling for swarms of ocean vehicles," in *Springer Handbook of Ocean Engineering: Autonomous Ocean Vehicles, Subsystems and Control*, T. Curtin, Ed. Springer, 2016, ch. 21, pp. 481–498.

[3] P. F. J. Lermusiaux, D. N. Subramani, J. Lin, C. S. Kulkarni, A. Gupta, A. Dutt, T. Lolla, P. J. Haley, Jr., W. H. Ali, C. Mirabito, and S. Jana, "A future for intelligent autonomous ocean observing systems," *Journal of Marine Research*, vol. 75, no. 6, pp. 765–813, Nov. 2017, the Sea. Volume 17, The Science of Ocean Prediction, Part 2.

[4] S. Aggarwal and N. Kumar, "Path planning techniques for unmanned aerial vehicles: A review, solutions, and challenges," *Computer communications*, vol. 149, pp. 270–299, 2020.

[5] M. Cococcioni, L. Fiaschi, and P. F. J. Lermusiaux, "Game theory for unmanned vehicles path planning in the marine domain: State of the art and new possibilities," *Journal of Marine Science and Engineering*, vol. 9, no. 11, 2021, special Issue on Machine Learning and Remote Sensing in Ocean Science and Engineering.

[6] A. A. Pereira, J. Binney, G. A. Hollinger, and G. S. Sukhatme, "Risk-aware path planning for autonomous underwater vehicles using predictive ocean models," *Journal of Field Robotics*, vol. 30, no. 5, pp. 741–762, 2013.

[7] Ü. Öztürk, M. Akdağ, and T. Ayabakan, "A review of path planning algorithms in maritime autonomous surface ships: Navigation safety perspective," *Ocean Engineering*, vol. 251, p. 111010, 2022.

[8] M.-G. Jeong, E.-B. Lee, M. Lee, and J.-Y. Jung, "Multi-criteria route planning with risk contour map for smart navigation," *Ocean Engineering*, vol. 172, pp. 72–85, 2019.

[9] G. Mannarini, N. Pinardi, M. Scuro, and L. Carelli, "Ship routing hazard maps," 2019.

[10] A. Doering, M. Wiggert, H. Krasowski, M. Doshi, P. F. J. Lermusiaux, and C. J. Tomlin, "Stranding risk for underactuated vessels in complex ocean currents: Analysis and controllers," in *2023 IEEE 62nd Conference on Decision and Control (CDC)*. Singapore: IEEE, Dec. 2023.

[11] D. Hentzen, M. Kamgarpour, M. Soler, and D. González-Arribas, "On maximizing safety in stochastic aircraft trajectory planning with uncertain thunderstorm development," *Aerospace Science and Technology*, vol. 79, pp. 543–553, 2018.

[12] R. K. Nichols, H. Mumm, W. D. Lonstein, J. J. Ryan, C. M. Carter, J.-P. Hood, J. S. Shay, R. W. Mai, M. J. Jackson *et al.*, *Unmanned vehicle systems & operations on air, sea, land*. New Prairie Press, 2020.

[13] T. A. Johansen and T. Perez, "Unmanned aerial surveillance system for hazard collision avoidance in autonomous shipping," in *2016 International Conference on Unmanned Aircraft Systems (ICUAS)*. IEEE, 2016, pp. 1056–1065.

[14] B. Zhang, L. Tang, and M. Roemer, "Probabilistic weather forecasting analysis for unmanned aerial vehicle path planning," *Journal of Guidance, Control, and Dynamics*, vol. 37, no. 1, pp. 309–312, 2014.

[15] Z. Niu, X. S. Shen, Q. Zhang, and Y. Tang, "Space-air-ground integrated vehicular network for connected and automated vehicles: Challenges and solutions," *Intelligent and Converged Networks*, vol. 1, no. 2, pp. 142–169, 2020.

[16] F. Chai, K. S. Johnson, H. Claustre, X. Xing, Y. Wang, E. Boss, S. Riser, K. Fennel, O. Schofield, and A. Sutton, "Monitoring ocean biogeochemistry with autonomous platforms," *Nature Reviews Earth & Environment*, vol. 1, no. 6, pp. 315–326, 2020.

[17] S. Baruah, P. Lee, P. Sarathy, and M. Wolf, "Achieving resiliency and behavior assurance in autonomous navigation: An industry perspective," *Proceedings of the IEEE*, vol. 108, no. 7, pp. 1196–1207, 2020.

[18] T. Yang, Z. Jiang, R. Sun, N. Cheng, and H. Feng, "Maritime search and rescue based on group mobile computing for unmanned aerial vehicles and unmanned surface vehicles," *IEEE transactions on industrial informatics*, vol. 16, no. 12, pp. 7700–7708, 2020.

[19] M. M. Marques, V. Lobo, A. P. Aguiar, J. E. Silva, J. B. de Sousa, M. de Fátima Nunes, R. A. Ribeiro, A. Bernardino, G. Cruz, and J. S. Marques, "An unmanned aircraft system for maritime operations: The automatic detection subsystem," *Marine Technology Society Journal*, vol. 55, no. 1, pp. 38–49, 2021.

[20] A. Farinha, J. Di Tria, R. Zufferey, S. F. Armanini, and M. Kovac, "Challenges in control and autonomy of unmanned aerial-aquatic vehicles," in *2021 29th Mediterranean Conference on Control and Automation (MED)*. IEEE, 2021, pp. 937–942.

[21] C. Ke and H. Chen, "Cooperative path planning for air–sea heterogeneous unmanned vehicles using search-and-tracking mission," *Ocean Engineering*, vol. 262, p. 112020, 2022.

[22] J. Wu, R. Li, J. Li, M. Zou, and Z. Huang, "Cooperative unmanned surface vehicles and unmanned aerial vehicles platform as a tool for coastal monitoring activities," *Ocean & Coastal Management*, vol. 232, p. 106421, 2023.

[23] M. C. Santos, B. Bartlett, V. E. Schneider, F. Ó. Brádaigh, B. Blanck, P. C. Santos, P. Trslic, J. Riordan, and G. Dooly, "Cooperative unmanned aerial and surface vehicles for extended coverage in maritime environments," *IEEE Access*, 2024.

[24] S. M. LaValle, *Planning algorithms*. Cambridge university press, 2006.

[25] A. Tsourdos, B. White, and M. Shanmugavel, *Cooperative path planning of unmanned aerial vehicles*. John Wiley & Sons, 2010.

[26] J.-C. Latombe, *Robot motion planning*. Springer Science & Business Media, 2012, vol. 124.

[27] T. Lolla, P. F. J. Lermusiaux, M. P. Ueckermann, and P. J. Haley, Jr., "Time-optimal path planning in dynamic flows using level set equations: Theory and schemes," *Ocean Dynamics*, vol. 64, no. 10, pp. 1373–1397, 2014.

[28] T. Lolla, P. J. Haley, Jr., and P. F. J. Lermusiaux, "Time-optimal path planning in dynamic flows using level set equations: Realistic applications," *Ocean Dynamics*, vol. 64, no. 10, pp. 1399–1417, 2014.

[29] M. Doshi, M. Bhabra, M. Wiggert, C. J. Tomlin, and P. F. J. Lermusiaux, "Hamilton–Jacobi multi-time reachability," in *2022 IEEE 61st Conference on Decision and Control (CDC)*, Cancún, Mexico, Dec. 2022, pp. 2443–2450.

[30] D. N. Subramani and P. F. J. Lermusiaux, "Energy-optimal path planning by stochastic dynamically orthogonal level-set optimization," *Ocean Modeling*, vol. 100, pp. 57–77, 2016.

[31] M. M. Doshi, M. S. Bhabra, and P. F. J. Lermusiaux, "Energy-time optimal path planning in dynamic flows: Theory and schemes," *Computer Methods in Applied Mechanics and Engineering*, vol. 405, p. 115865, Feb. 2023.

[32] T. Lolla, P. J. Haley, Jr., and P. F. J. Lermusiaux, "Path planning in multiscale ocean flows: Coordination and dynamic obstacles," *Ocean Modelling*, vol. 94, pp. 46–66, 2015.

[33] W. Sun, P. Tsiotras, T. Lolla, D. N. Subramani, and P. F. J. Lermusiaux, "Multiple-pursuer-one-evader pursuit evasion game in dynamic flow fields," *Journal of Guidance, Control and Dynamics*, vol. 40, no. 7, Apr. 2017.

[34] C. Mirabito, D. N. Subramani, T. Lolla, P. J. Haley, Jr., A. Jain, P. F. J. Lermusiaux, C. Li, D. K. P. Yue, Y. Liu, F. S. Hover, N. Pulsone, J. Edwards, K. E. Railey, and G. Shaw, "Autonomy for surface ship interception," in *Oceans '17 MTS/IEEE Conference*, Aberdeen, Jun. 2017.

[35] C. S. Kulkarni and P. F. J. Lermusiaux, "Three-dimensional time-optimal path planning in the ocean," *Ocean Modelling*, vol. 152, Aug. 2020.

[36] D. N. Subramani, Q. J. Wei, and P. F. J. Lermusiaux, "Stochastic time-optimal path-planning in uncertain, strong, and dynamic flows," *Computer Methods in Applied Mechanics and Engineering*, vol. 333, pp. 218–237, 2018.

[37] D. N. Subramani and P. F. J. Lermusiaux, "Risk-optimal path planning in stochastic dynamic environments," *Computer Methods in Applied Mechanics and Engineering*, vol. 353, pp. 391–415, Aug. 2019.

[38] M. Wiggert, M. Doshi, P. F. J. Lermusiaux, and C. J. Tomlin, "Navigating underactuated agents by hitchhiking forecast flows," in *2022 IEEE 61st Conference on Decision and Control (CDC)*, Cancún, Mexico, Dec. 2022, pp. 2417–2424.

[39] M. S. Bhabra, M. Doshi, B. C. Koenig, P. J. Haley, Jr., C. Mirabito, P. F. J. Lermusiaux, C. A. Goudey, J. Curcio, D. Manganelli, and H. Goudey, "Optimal harvesting with autonomous tow vessels for offshore macroalgae farming," in *OCEANS 2020 IEEE/MTS*. IEEE, Oct. 2020, pp. 1–10.

[40] M. Killer, M. Wiggert, H. Krasowski, M. Doshi, P. F. J. Lermusiaux, and C. J. Tomlin, "Maximizing seaweed growth on autonomous farms: A dynamic programming approach for underactuated systems operating in uncertain ocean currents," in *41st IEEE Conference on Robotics and Automation (ICRA 2024)*. Yokohama: IEEE, May 2024, sub-judice.

[41] D. L. Ferris, D. N. Subramani, C. S. Kulkarni, P. J. Haley, and P. F. J. Lermusiaux, "Time-optimal multi-waypoint mission planning in dynamic environments," in *OCEANS Conference 2018*. Charleston, SC: IEEE, Oct. 2018.

[42] G. Mannarini, D. N. Subramani, P. F. J. Lermusiaux, and N. Pinardi, "Graph-search and differential equations for time-optimal vessel route planning in dynamic ocean waves," *IEEE Transactions on Intelligent Transportation Systems*, vol. 21, no. 6, pp. 1–13, Jun. 2020.

[43] D. N. Subramani, P. F. J. Lermusiaux, P. J. Haley, Jr., C. Mirabito, S. Jana, C. S. Kulkarni, A. Girard, D. Wickman, J. Edwards, and J. Smith, "Time-optimal path planning: Real-time sea exercises," in *Oceans '17 MTS/IEEE Conference*, Aberdeen, Jun. 2017.

[44] J. Edwards, J. Smith, A. Girard, D. Wickman, D. N. Subramani, C. S. Kulkarni, P. J. Haley, Jr., C. Mirabito, S. Jana, and P. F. J. Lermusiaux, "Data-driven learning and modeling of AUV operational characteristics for optimal path planning," in *Oceans '17 MTS/IEEE Conference*, Aberdeen, Jun. 2017.

[45] P. F. J. Lermusiaux, P. J. Haley, Jr., S. Jana, A. Gupta, C. S. Kulkarni, C. Mirabito, W. H. Ali, D. N. Subramani, A. Dutt, J. Lin, A. Shcherbina, C. Lee, and A. Gangopadhyay, "Optimal planning and sampling predictions for autonomous and Lagrangian platforms and sensors in the northern Arabian Sea," *Oceanography*, vol. 30, no. 2, pp. 172–185, Jun. 2017, special issue on Autonomous and Lagrangian Platforms and Sensors (ALPS).

[46] P. F. J. Lermusiaux, P. J. Haley, Jr., C. Mirabito, E. M. Mule *et al.*, "Real-time ocean probabilistic forecasts, reachability analysis, and adaptive sampling in the Gulf of Mexico," in *OCEANS 2024 IEEE/MTS Halifax*. Halifax: IEEE, Sep. 2024, in press.

[47] E. M. Mule, P. J. Haley, Jr., C. Mirabito, P. F. J. Lermusiaux *et al.*, "Real-time probabilistic reachability forecasting for gliders in the Gulf of Mexico," in *OCEANS 2024 IEEE/MTS Halifax*. Halifax: IEEE, Sep. 2024, in press.

[48] M. S. Bhabra, "Harvest-time optimal path planning in dynamic flows," Master's thesis, Massachusetts Institute of Technology, Department of Mechanical Engineering and Computational Science & Engineering, Cambridge, Massachusetts, Sep. 2021.

[49] M. S. Bhabra, M. Doshi, and P. F. J. Lermusiaux, "Harvest-time optimal path planning in dynamic flows," 2024, in preparation.

[50] N. Gavrilovic, J.-M. Moschetta, and Q. Barascud, "Development of a Hydrogen-powered UAV System for Crossing the Atlantic Ocean," in *AIAA SCITECH 2023 Forum*. National Harbor, MD & Online: American Institute of Aeronautics and Astronautics, Jan. 2023. [Online]. Available: https://arc.aiaa.org/doi/10.2514/6.2023-1924

[51] N. Gavrilovic, D. Vincekovic, and J. Moschetta, "A long range fuel cell/soaring uav system for crossing the atlantic ocean," in *11th international micro air vehicle competition and conference, madrid, Spain. IMAV*, 2019, p. 121e31.

[52] MSEAS NESMA Ex., "New England Seamounts Experiment Acoustics (NESMA) 2024: New England Seamount Chain – July, 2024," Jul. 2024. [Online]. Available: http://mseas.mit.edu/Sea_exercises/NESMA/

[53] J. F. Lawless, *Statistical models and methods for lifetime data*. John Wiley & Sons, 2011.

[54] J. O'Quigley *et al.*, *Survival Analysis*. Springer, 2021.

[55] P. J. Haley, Jr. and P. F. J. Lermusiaux, "Multiscale two-way embedding schemes for free-surface primitive equations in the "Multidisciplinary Simulation, Estimation and Assimilation System"," *Ocean Dynamics*, vol. 60, no. 6, pp. 1497–1537, Dec. 2010.

[56] P. J. Haley, Jr., A. Agarwal, and P. F. J. Lermusiaux, "Optimizing velocities and transports for complex coastal regions and archipelagos," *Ocean Modelling*, vol. 89, pp. 1–28, May 2015.

[57] J. Borges de Sousa, K. H. Johansson, J. Silva, and A. Speranzon, "A verified hierarchical control architecture for co-ordinated multi-vehicle operations," *International Journal of Adaptive Control and Signal Processing*, vol. 21, no. 2-3, pp. 159–188, 2007.

[58] K. Rajan, F. Aguado, P. Lermusiaux, J. B. de Sousa, A. Subramaniam, and J. Tintore, "METEOR: A Mobile (portable) ocEan roboTic obsErvatORy," *Marine Technology Society Journal*, vol. 55, no. 3, pp. 74–75, May 2021.

[59] J. P. Heuss, P. J. Haley, Jr., C. Mirabito, E. Coelho, M. C. Schönau, K. Heaney, and P. F. J. Lermusiaux, "Reduced order modeling for stochastic prediction onboard autonomous platforms at sea," in *OCEANS 2020 IEEE/MTS*. IEEE, Oct. 2020, pp. 1–10.

[60] T. Ryu, J. P. Heuss, P. J. Haley, Jr., C. Mirabito, E. Coelho, P. Hursky, M. C. Schönau, K. Heaney, and P. F. J. Lermusiaux, "Adaptive stochastic reduced order modeling for autonomous ocean platforms," in *OCEANS 2021 IEEE/MTS*. IEEE, Sep. 2021, pp. 1–9.

[61] T. Ryu, W. H. Ali, P. J. Haley, Jr., C. Mirabito, A. Charous, and P. F. J. Lermusiaux, "Incremental low-rank dynamic mode decomposition model for efficient dynamic forecast dissemination and onboard forecasting," in *OCEANS 2022 IEEE/MTS*. Hampton Roads, VA: IEEE, Oct. 2022, pp. 1–8.

[62] M. Tieppo, E. Pereira, L. González Garcia, M. Rolim, E. Castanho, A. Matos, A. Silva, B. Ferreira, M. Pascoal, E. Almeida, F. Costa, F. Zabel, J. Faria, J. Azevedo, J. Alves, J. Moutinho, L. Gonçalves, M. Martins, N. Cruz, N. Abreu, P. Silva, R. Viegas, S. Jesus, T. Chen, T. Miranda, A. Papalia, D. Hart, J. Leonard, M. Haji, O. de Weck, P. Godart, and P. Lermusiaux, "Submarine cables as precursors of persistent systems for large scale oceans monitoring and autonomous underwater vehicles operation," in *OCEANS 2022 IEEE/MTS*. Hampton Roads, VA: IEEE, Oct. 2022, pp. 1–7.

[63] E. Pereira, M. Tieppo, J. a. Faria, D. Hart, P. Lermusiaux, and The K2D Project Team, "Subsea cables as enablers of a next generation global ocean sensing system," *Oceanography*, vol. 36, no. Supp. 1, Feb. 2023, special issue: "Frontiers in Ocean Observing: Emerging Technologies for Understanding and Managing a Changing Ocean".